ADVANCED MATERIALS
www.advmat.de

Tailored Graphene Micropatterns by Wafer-Scale Direct Transfer for Flexible Chemical Sensor Platform

Yeonhoo Kim, Taehoon Kim, Jinwoo Lee, Yong Seok Choi, Joonhee Moon, Seo Yun Park, Tae Hyung Lee, Hoon Kee Park, Sol A Lee, Min Sang Kwon, Hyung-Gi Byun, Jong-Heun Lee, Myoung-Gyu Lee, Byung Hee Hong,* and Ho Won Jang**

2D materials, such as graphene, exhibit great potential as functional materials for numerous novel applications due to their excellent properties. The grafting of conventional micropatterning techniques on new types of electronic devices is required to fully utilize the unique nature of graphene. However, the conventional lithography and polymer-supported transfer methods often induce the contamination and damage of the graphene surface due to polymer residues and harsh wet-transfer conditions. Herein, a novel strategy to obtain micropatterned graphene on polymer substrates using a direct curing process is demonstrated. Employing this method, entirely flexible, transparent, well-defined self-activated graphene sensor arrays, capable of gas discrimination without external heating, are fabricated on 4 in. wafer-scale substrates. Finite element method simulations show the potential of this patterning technique to maximize the performance of the sensor devices when the active channels of the 2D material are suspended and nanoscaled. This study contributes considerably to the development of flexible functional electronic devices based on 2D materials.

Emerging new technologies, such as flexible, foldable, transparent, and wearable devices, can reshape human lives and industries. Metals and semiconducting metal oxides have been employed as primary materials for conventional electronic devices to date, but these materials are brittle and nontransparent. On the contrary, 2D materials, such as graphene, can offer novel opportunities to realize new types of electronics by providing their unique properties, such as flexibility, transparency, and tunable electrical properties.[1–7] Graphene is the most representative 2D material and has been studied with great interest. It has been applied in diverse sensing applications, including biological and chemical sensors, owing to its unique properties, such as a high surface-to-volume ratio, easy surface modification, transparency, and flexibility.[8–10] The dangling bonds and defects on basal planes and edge sites of graphene provide opportunities to modify surface chemistry, which play a key role in fabricating high-performance chemical sensor arrays that are equipped with the ability to discriminate target chemical species. However, embedding graphene into flexible devices remains a challenge due to difficulties in microscale patterning of graphene on flexible substrates, such as a polymer.

Dr. Y. Kim, T. Kim, Dr. S. Y. Park, T. H. Lee, Dr. H. K. Park, S. A Lee, Prof. M. S. Kwon, Prof. M.-G. Lee, Prof. H. W. Jang
Department of Materials Science and Engineering
Research Institute of Advanced Materials
Seoul National University
Seoul 08826, Republic of Korea
E-mail: myounglee@snu.ac.kr; hwjang@snu.ac.kr

Dr. Y. Kim
Center for Integrated Nanotechnologies
Los Alamos National Laboratory
Los Alamos, NM 87544, USA

Dr. J. Lee
Materials Deformation Department
Korea Institute of Materials Science
Changwon 51508, Republic of Korea

Dr. Y. S. Choi, Prof. B. H. Hong
Graphene Research Center and Graphene Square Inc.
Advanced Institute of Convergence Technology
Seoul National University
Suwon 16229, Republic of Korea

Dr. J. Moon
Research Center for Materials Analysis
Korea Basic Science Institute
Gwahak-ro, Yuseong-gu, Daejeon 34133, Republic of Korea

Prof. H.-G. Byun
Division of Electronics
Information and Communication Engineering
Kangwon National University
Samcheok 25913, Republic of Korea

Prof. J.-H. Lee
Department of Materials Science and Engineering
Korea University
Seoul 02841, Republic of Korea

Prof. B. H. Hong
Department of Chemistry
Seoul National University
Seoul 08826, Republic of Korea
E-mail: byunghee@snu.ac.kr

The ORCID identification number(s) for the author(s) of this article can be found under https://doi.org/10.1002/adma.202004827.

DOI: 10.1002/adma.202004827

For micropatterning graphene-based materials on flexible substrates, diverse patterning strategies have been explored.[11–16] El-Kady and Kaner patterned reduced graphene oxide (rGO) on polymer substrates by laser scribing.[15] He et al. fabricated rGO-based field-effect transistor sensors by the polydimethylsiloxane (PDMS) moulding method.[16] Moreover, various inkjet printing methods, which employ a slurry of graphene derivatives, have been widely reported.[12,17–20] Despite these efforts, microscale patterning (narrower than 5 μm) of chemical vapor deposited (CVD) graphene, with a controlled number of layers, on flexible substrates has never been achieved. This is because graphene layers are too thin to endure harsh conditions in multistep wet fabrication processes.

Here, we establish a novel strategy to micropattern 2D materials onto flexible substrates. Polymer is employed to hold graphene micropatterns and to act as a flexible substrate simultaneously. This method is called direct polymer curing (DPC) transfer. To demonstrate the reliability and durability of the micropatterning and transfer processes, entirely flexible and transparent graphene sensor arrays were fabricated on 4 in. polymer wafer-scale substrates. Patterned graphene microchannels were capable of self-heating by an applied bias voltage of less than 9 V. The sensor arrays comprised four single sensors, which have surface decoration with different noble metals. The arrays successfully classified target gases without external heating.

A schematic illustration of the DPC transfer process is presented in **Figure 1**a. Prior to the DPC transfer process, graphene is synthesized by CVD and stacked on Cu foil to make three-layer graphene (3LG) to obtain enough self-heating.[21] The 3LG on the Cu foil is then directly patterned by photolithography. The graphene layer not covered by photoresist (PR) is etched by oxygen reactive ion etching (RIE), and an acetone treatment removes the PR layer covering the micropatterned graphene layer. Next, transparent polyimide (PI) varnish is spin-coated and directly cured on top of the patterned graphene by thermal annealing at 300 °C. The key idea of DPC transfer is to use polymer as a transfer medium and flexible substrate simultaneously. We assumed that micropatterns of 2D materials, which are extremely difficult to define on flexible substrates, would be well-defined if the polymer layer is simultaneously employed as the final flexible substrate. Other polymers such as poly(methyl methacrylate) (PMMA), PDMS, and polystyrene (PS) can be used as the polymer layer (Figure S1, Supporting Information), but PI with a high glass transition temperature is used to endure the high temperature by self-heating. To make devices more stable, a thermal laminating film (TF) can be laminated on the cured polymer/graphene/Cu foil as a supporting substrate. In the final step of the process, Cu foil is etched using an ammonium persulfate (APS) solution reveal graphene micropatterns.

Optical images for each processing step are shown in Figure 1b,c. Well-developed micropatterned PR on graphene/Cu foil via photolithography process is visible in Figure 1b. Four types of patterns with microchannels of different dimensions were defined on the foil (Figure S2, Supporting Information). The lengths of the microchannels (L_c) were designed to be 0.05, 0.1, 0.25, and 0.5 mm, respectively, and the width of the microchannels (W_c) was fixed at 5 μm. After the supporting layer lamination and Cu etching processes, micropatterned graphene arrays on a PI substrate were entirely transparent and flexible (Figure 1c). These patterning processes were conducted on 4 in. wafer-scale Cu foil, and the final devices were transparent (Figure S3, Supporting Information). Transmittance was measured to be ≈80% for the graphene/PI sample and ≈60% after attachment of a TF on the graphene/PI sample (Figure S4, Supporting Information).

Graphene microchannels on the polymer substrates were characterized by Raman spectroscopy (Figure 1d; Figure S5, Supporting Information). To characterize the graphene on the polyimide substrate, confocal Raman spectroscopy (Raman force, Nanophoton) was performed using a 532 nm laser with a power of 1 mW. The Raman spectra of the PI and the graphene channel on the PI are shown in Figure 1d. Strong peaks of PI represent the C=O stretch at 1786 cm^{-1}, C−N−C axial vibration stretch at 1395 cm^{-1}, and C−N−C transverse vibration stretch at 1124 cm^{-1}.[22] The Raman G peak and the 2D peak of graphene appear at 1580 and 2694 cm^{-1}, respectively, which typically come from the bond stretching and ring breathing modes, respectively.[23] The Raman map exhibits 2D surface information of large-scale graphene patterned on the PI substrate, which was plotted with the 2D peak of graphene. The clear dark-gray region of the Raman map indicates that graphene is successfully patterned on the PI substrate and the graphene channel length is ≈100 μm.

An important component of DPC transfer is no contamination of 2D materials during the micropatterning process and transfer process. Diverse polymers have been explored for ultra-clean and damage-free graphene transfer, but surface contaminations by the photolithography process such as PR residues is inevitable.[24,25] On the contrary, graphene layers are transferred reversely onto cured polymer substrates in the DPC method; therefore, the graphene surface contacted to the copper foil side becomes top surface in the final step, which has not been exposed to any impurities such as PR and PMMA. In the conventional polymer-supported transfer method, since the PMMA-coated graphene patterns floating on deionized (DI) water are scooped with the polymer substrate, the contaminated graphene surface with polymer residues becomes the top side of the final device after PMMA removal (Figure S6a,b, Supporting Information). Atomic force microscopy (AFM) images in Figure 1e,f show that the graphene transferred by the DPC transfer method has very clean surface, whereas the graphene transferred by the conventional transfer method has many polymer residues on the surface, which have been a major drawback of photolithography and PMMA transfer of 2D materials.[26–30] X-ray photoemission spectroscopy (XPS) and energy dispersive spectroscopy (EDS) analysis confirmed that Cu has been completely removed by the APS-based etching process (Figure S7, Supporting Information).

All devices with the graphene microchannels of 5 μm width and 0.05 mm length were examined to investigate the stability and reliability of the wafer-scale patterning process. The microchannels of all 30 devices were formed without any disconnected channels, and the average resistance was calculated to be 12.03 kOhm with a 19.09% relative standard deviation (Table S1, Supporting Information). Figure 1g displays a 2D color map of the resistance for 30 graphene microchannels patterned on a flexible substrate and the uniform green color near ≈12 kOhm on the map demonstrated the reliability of the DPC transfer for micropatterning 2D materials.

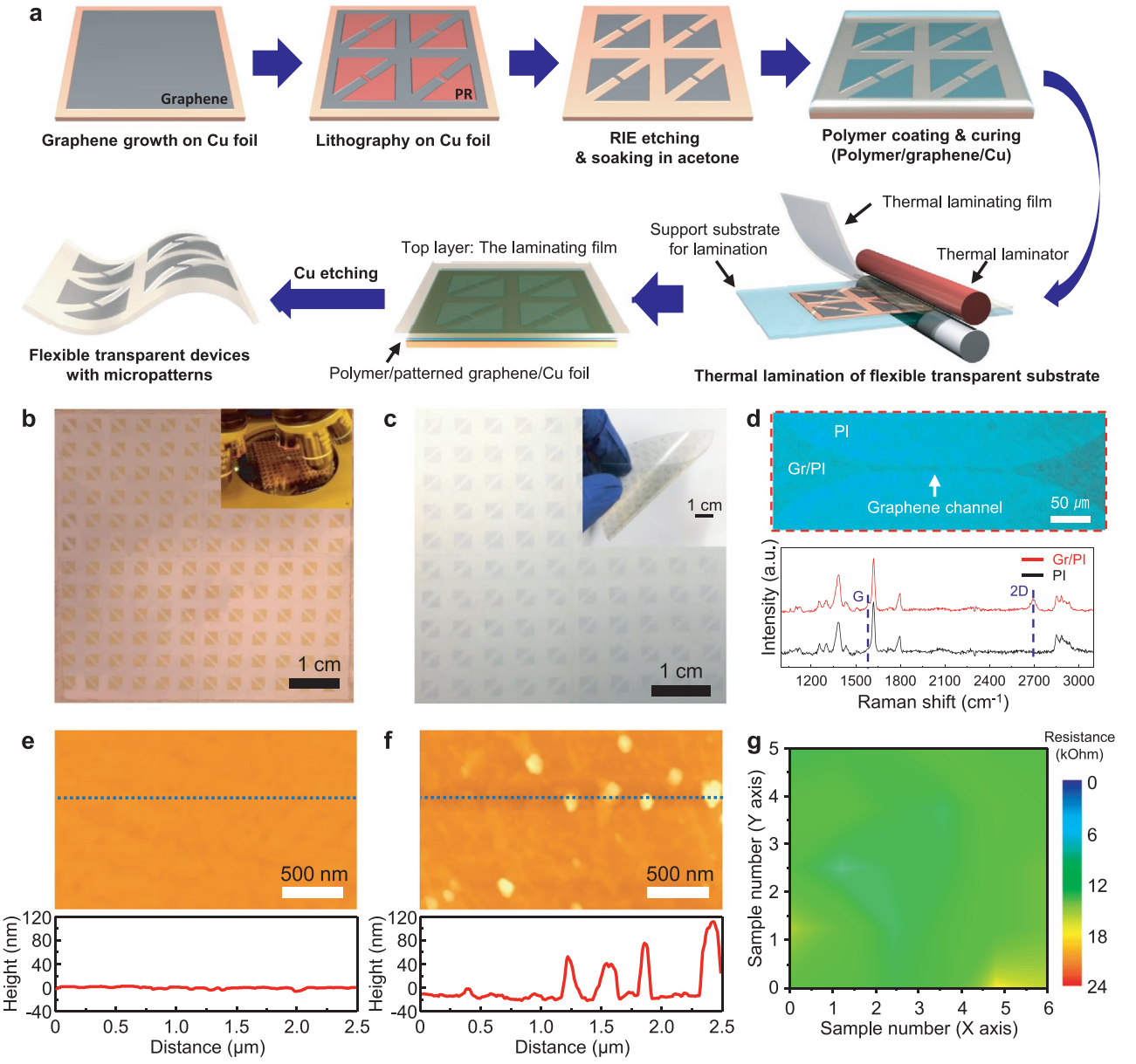

Figure 1. Fabrication of micropatterned graphene arrays on flexible substrates via DPC transfer. a) Schematic illustration of DPC transfer for micro-scale patterning of graphene on flexible transparent substrates. b) Micropatterned PR on graphene/Cu foil. Inset shows the photolithography process. c) Graphene micropatterns on 4 in. wafer-scale flexible substrate. Inset shows the entirely flexible and transparent graphene array. d) Raman analysis of graphene layers (Gr) on polyimide substrate (PI). AFM images of the graphene film on the polymer substrate transferred by e) the DPC transfer method and f) the polymer-supported transfer method. Surface profiles through the blue dotted lines are shown (down). g) 2D color mapping of resistances for 30 graphene micropatterns on a flexible substrate.

I–*V* characteristics were measured for the graphene arrays along the L_c ranging from 0.05 to 0.5 mm, with the fixed W_c at 5 μm (**Figure 2**a). Graphene arrays show ohmic behavior regardless of L_c since the arrays are composed of only graphene and do not have a heterojunction. Power, as a function of the applied voltage, is presented in Figure 2b. The power of graphene microchannels is expected to abruptly increase following the equation $P = V^2/R$, which is depicted with dashed lines in Figure 2b. However, due to the self-heating effect in the graphene microchannels, the resistance of the devices simultaneously increased as the applied voltage gradually increased (Figure 2c). The dependence of resistance on the L_c of the devices and the apparent temperature is presented in Figure S8 in the Supporting Information. As a result, the power consumption is much lower than the expected power consumption, which broadens the potential of the self-heating graphene arrays for low power consumption sensor devices.

The self-heating effect of a graphene device with $L_c = 0.05$ mm was observed using an infrared camera (Figure 2d). The apparent temperature increased up to 68.1 °C at 9 V, and the deformation of

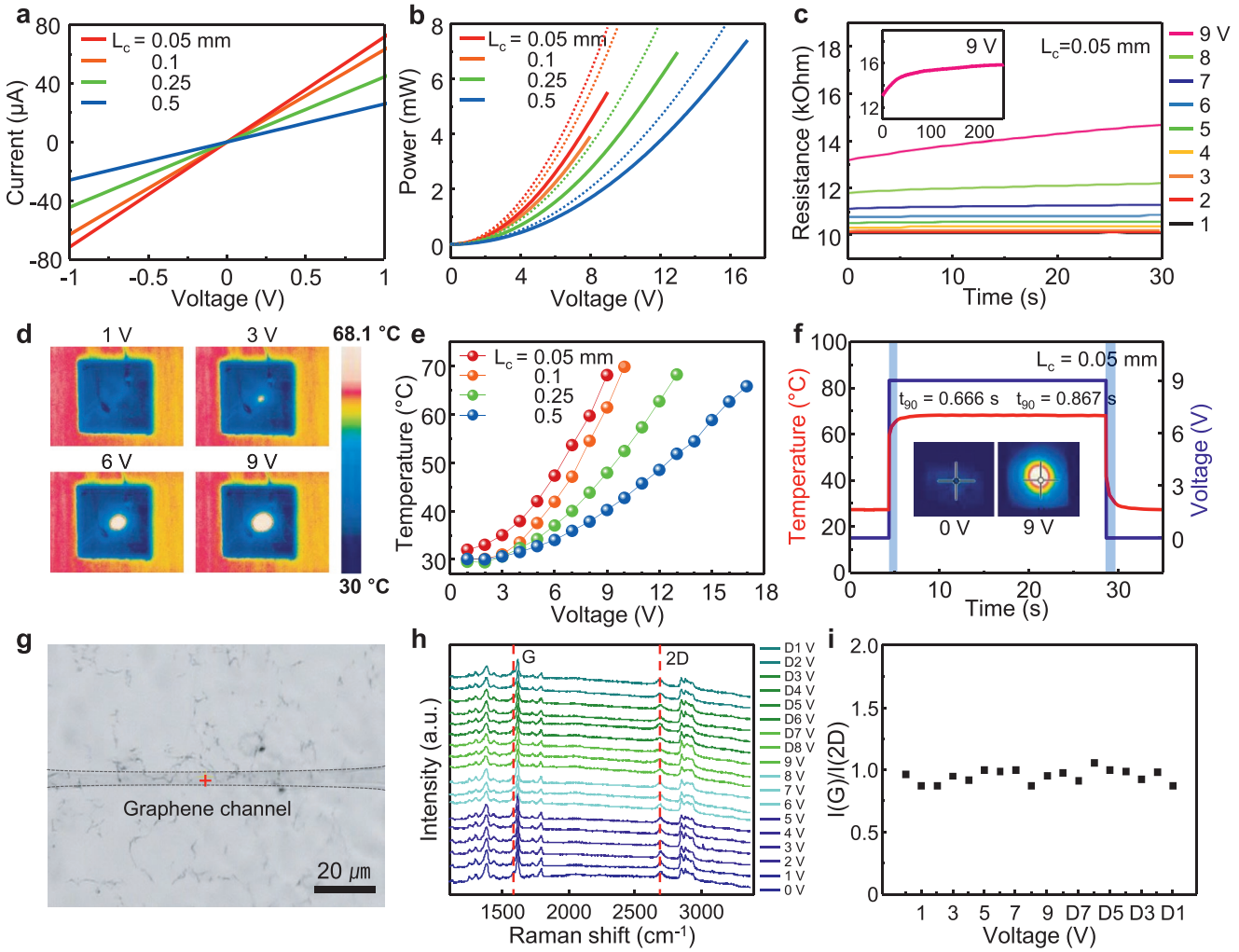

Figure 2. Electrical and self-heating characteristics of graphene microchannels. a) *I–V* characteristics of graphene microchannel with different channel lengths. b) Power as a function of voltages with different channel lengths. The dashed lines present expected curves for devices following equation of $P = V^2/R$. c) Resistances of the device with $L_c = 0.05$ mm as a function of applied voltages. d) Thermographic images of the device with $L_c = 0.05$ mm during self-heating. e) Temperature of the devices with different channel lengths as a function of voltages. f) Heating temperature of the device with $L_c = 0.05$ mm as a function of time. g) A graphene microchannel observed by Raman system quipped with high-resolution optical microscope during self-heating. Raman spectra was recorded on the red cross-point on the graphene microchannel. h) Raman spectra of the graphene microchannel according to the applied bias voltages from 0 to 9 V and again 9 to 1 V. D V denotes the applied voltage after applying 9 V. i) The intensity ratio *I*(G)/*I*(2D) according to the applied bias voltages.

the PI substrate began at 10 V. The microscale graphene channels where the Joule heating is generated are too small to be resolved by the infrared camera we used. We believe that the real temperature at localized spots is expected to be much higher than the measured apparent temperature. In Figure 2e, the self-heating effect improved as L_c decreased. Joule heating in an electrical resistor can be expressed as $J \propto IV = V^2/R$, where J, I, and R denote the Joule heating effect, current, and resistance, respectively. Hence, when L_c decreases, R decreases, which enhances the Joule heating effect. A video was recorded to check the time required for the microchannels with $L_c = 0.05$ mm to be fully self-heated (Video S1, Supporting Information). Response and recovery times (response and recovery t_{90}) are defined as the time required for the apparent temperature to reach 90% of its steady-state value when voltage is applied and decreased, respectively. Response t_{90} and recovery t_{90} were 0.666 and 0.867 s, respectively (Figure 2f).

The key parameters of several graphene-based flexible heaters are listed in Table S2 in the Supporting Information. The graphene microchannel with L_c = 0.05 mm has a lower operating voltage and faster response time than other graphene-based materials prepared by various methods.[31–39] The extremely low power consumption of 5.5 mW, fast reactions in less than 1 s, and low operating voltage indicate the ultrahigh effective self-heating of the graphene microchannels on the flexible substrate.

To analyze the properties of the graphene microchannel on the PI substrate during self-heating, the stability of the graphene microchannel was investigated by in situ Raman spectroscopy. The optical image in Figure 2g shows the graphene channel (black dotted line) on the PI substrate. Raman spectra were recorded at the red plus sign in the middle of the graphene channel, as indicated in Figure 2g. The Raman peaks

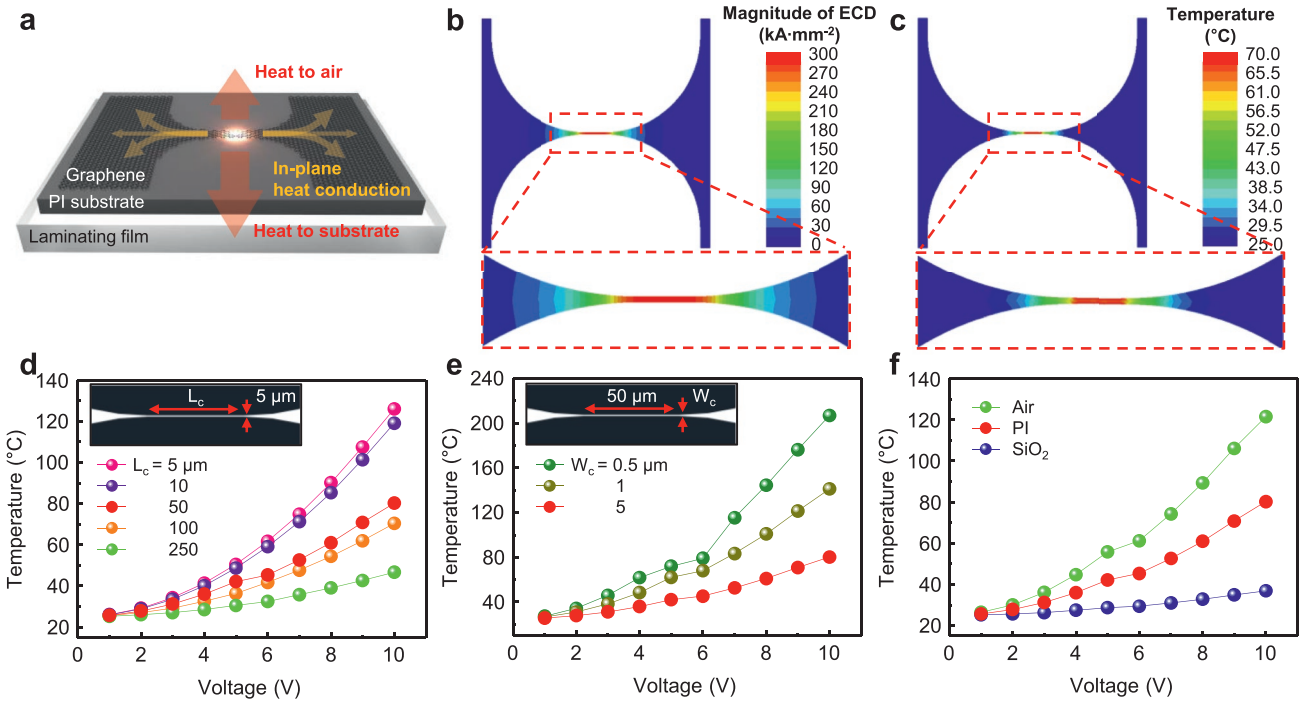

Figure 3. Finite element simulation of graphene microchannels. a) Finite element modeling of heat transfer simulation. b) Magnitude of electric current density from simulation. c) Temperature distribution from simulated results. Maximum temperatures as a function of voltages from sensitivity tests depending on d) channel length, e) channel width, and f) substrate materials.

of the micropatterned graphene showed no changes when the voltage was applied from 0 to 9 V and again from 9 to 1 V (Figure 2h). During the input of potential with the voltage profile presented in Figure 2h, positions of the G and 2D peaks did not change noticeably (Figure 2i). Optical images at each potential show that the surface morphology of graphene on PI was robustly maintained under 9 V (Figure S9, Supporting Information). The graphene channel maintained constant resistances at 1 and 9 V, respectively, after multiple heating and cooling cycles (Figure S10, Supporting Information). This clearly indicates that the graphene channel on PI possesses superior thermal and mechanical stability up to 9 V. However, when the potential increased more than 10 V, the surface morphology of the PI substrate changed gradually due to thermal energy, which induces a partially unfocused optical image of the graphene channel on the PI (Figure S11, Supporting Information). Moreover, the intensity of peaks from graphene in Raman spectra reduced gradually with increasing input potential. The graphene channel finally disappeared at 16 V.

Finite element (FE) modelling was performed to investigate further the self-heating properties of the tailored graphene microchannels (details are available in "Finite element simulations" section in the Supporting Information). For a reference condition, the process parameters of the FE simulation, such as the interface heat transfer coefficient, Joule heating fraction, and contact gap conductance, were determined by the best fit of the calculated maximum temperature to the experimentally measured temperature. These parameters are listed in Table S3 in the Supporting Information. The fraction η is set to unity, which assumes that the electrical work is completely converted to heat.[40] A schematic illustration of the FE simulation is depicted in **Figure 3**a. The reference condition for calibrating the FE model was: voltage = 9 V, L_c = 50 μm, and W_c = 5 μm. Figure 3b,c shows the magnitude of the electric current density and temperature distribution, respectively, for the reference simulation. The pertinent video files of temperature variation recorded from the finite element simulation are provided in Videos S2 and S3 in the Supporting Information. The calculated maximum temperature in the simulation agreed well with the experimentally measured temperature (70.9 vs 68.1 °C, respectively). The calculated convective heat loss rate obtained by the simulation was also in a reasonable range compared to other reported values.[41,42]

Numerical sensitivity analyses were carried out to investigate the effects of channel length, channel width, and type of substrate on the temperature increase. This analysis is also meaningful for projecting the potential temperature increase, which cannot be readily done by experiments. Figure 3d–f shows the predicted changes in the maximum temperature for the three parameters, L_c, W_c, and substrate materials. As can be seen in Figure 3d,e, the maximum temperature as a function of voltage increases with the decrease in L_c and W_c. However, the effects are not linear for voltage, and channel length and width. The increase in temperature can be interpreted as a higher current density for reduced channel dimensions. For example, the temperature is predicted to increase up to ≈200 °C for L_c = 50 μm and W_c = 0.5 μm. Figure 3f shows the maximum temperature for different substrate materials. Two different substrate materials, PI and SiO_2, and no substrate (air) were simulated. Without a substrate or when graphene is directly exposed to air, a significant temperature increase was predicted using a quadratic function of the applied voltage. In contrast, for the

SiO_2 substrate, an almost negligible temperature increase was predicted due to a high rate of heat transfer into air. These simulation results indicate that the temperature increase can be efficiently controlled by properly designing the geometry of graphene and the substrate material.

To demonstrate potential applications of DPC transfer, we fabricated an entirely transparent and flexible all-graphene chemoresistive sensor array. The sensor array comprised four single graphene sensors based on a pristine graphene microchannel and graphene microchannels decorated with Ag, Au, and Pt nanoparticles (**Figure 4**a). Noble metal decoration is a promising strategy to improve the selectivity of graphene-based gas sensors by modifying surface chemistry.[43] The graphene patterns with the microchannels of 5 µm width and 50 µm length were fabricated on a polymer substrate, and noble metals were deposited onto microchannels using a metal mask

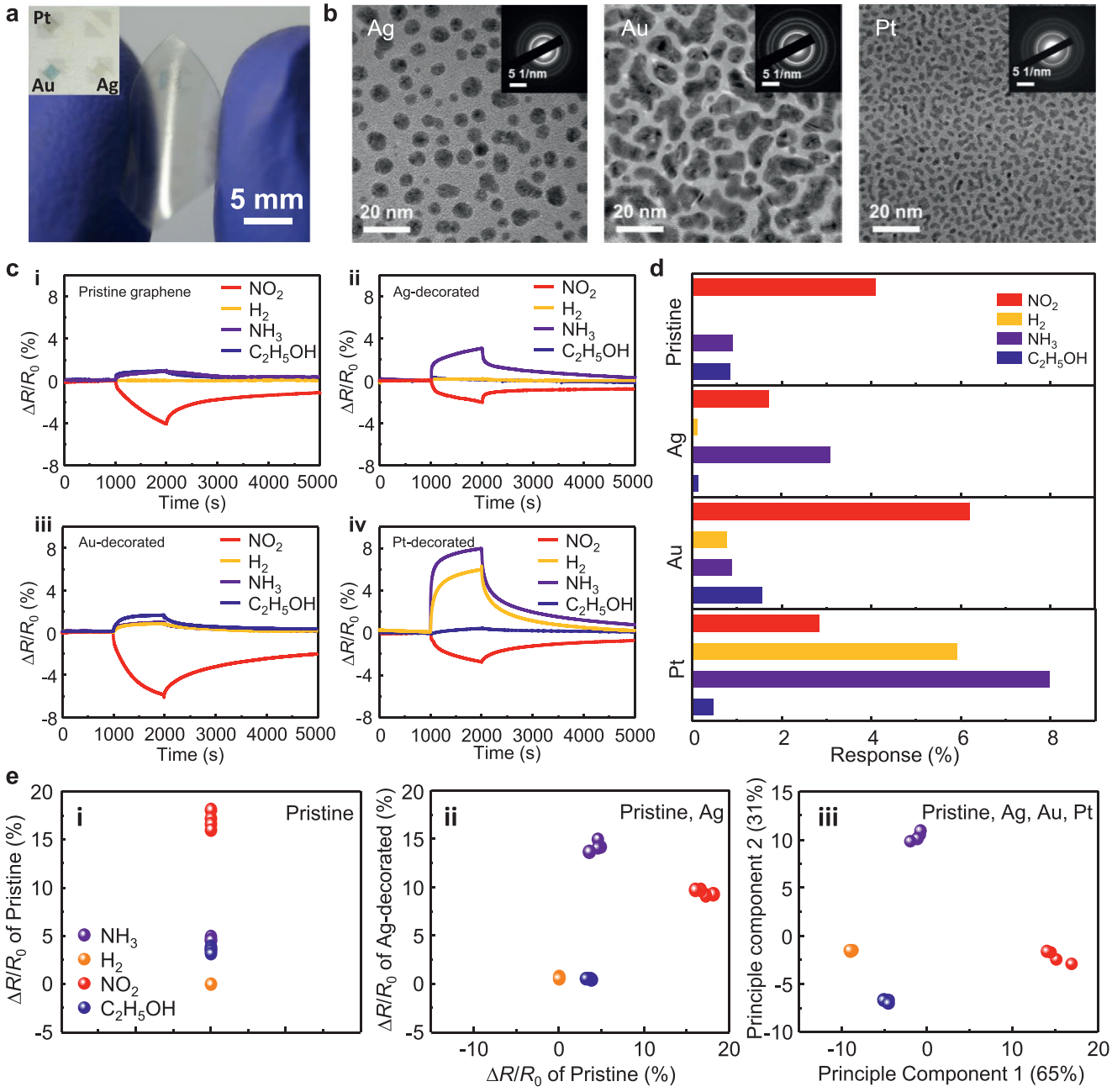

Figure 4. Chemoresistive sensing characterizations of the graphene sensor array. a) Optical images of flexible and transparent chemoresistive graphene sensor arrays with noble metal decorations. Inset shows the device on a white paper. b) TEM images of graphene layers decorated with Ag, Au, and Pt. c) Dynamic sensing transients of i) pristine graphene, graphene with ii) Ag, iii) Au, and iv) Pt decoration upon exposure to NH_3, H_2, C_2H_5OH, and NO_2. d) Gas sensing responses of the devices to the different gas species depending on decorated noble metals. e) Response profiles for four gases of i) pristine graphene sensor and ii) pristine and Ag-decorated graphene sensors, and iii) the PCA plot of pristine, Ag-decorated, Au-decorated, and Pt-decorated graphene sensors.

and e-beam evaporator (Figure S12, Supporting Information). The size of Ag, Au, and Pt nanoparticles deposited on graphene layers was measured to be ≈1–20 nm by transmission electron microscope (Figure 4b). Raman spectra confirmed that the graphene layers were not damaged during DPC transfer, RIE, or e-beam deposition (Figure S13, Supporting Information).

To verify the sensing performance, the sensor array was exposed to 50 ppm NH_3, 50 ppm H_2, 50 ppm C_2H_5OH, and 5 ppm NO_2 under the self-activated state at 9 V. The dynamic sensing transients of i) pristine graphene and graphene decorated with ii) Ag, iii) Au, and iv) Pt are displayed in Figure 4c. Our devices show good response and recovery without external heating or UV irradiation comparing with previous graphene-based sensors.[44,45] The response is defined as $(R_{gas} - R_{air})/R_{air} \times 100$, where R_{air} and R_{gas} are the resistance of the sensor exposed to the dry air and test gases, respectively. Each sensor shows distinct sensing characteristics upon exposure to different gases (Figure 4d). Pristine graphene shows the highest response to the oxidizing NO_2 gas. Ag-decorated graphene shows the highest response to the reducing NH_3 gas and also detects NO_2. Au-decorated graphene has the highest response to NO_2, but very interestingly, it shows higher response to the reducing C_2H_5OH gas than reducing H_2 and NH_3 gases. This provides a clue to develop volatile organic compounds sensors using graphene, which has been proven to be challenging.[46] Pt-decorated graphene shows similar high responses to NH_3 and H_2. A 3D bar chart is presented to clearly compare the varied sensing responses of each sensor (Figure S14, Supporting Information).

Chemoresistive gas sensing relies on the electrical resistance change of the graphene channel caused by the changes in carrier concentration or mobility of the sensing material, graphene, upon exposure to the target gas. The rise or fall in resistance mainly depend on the charge transfer between adsorbed gas molecules and graphene (details are available in "Gas sensing mechanism" section in the Supporting Information).

One of the main purposes of designing sensor arrays is gas selectivity. A sensor array comprised single sensors provides different sensing information and can differentiate target chemical species.[47–49] To classify the gas species, the principal component analysis (PCA) was conducted using sensing responses and response times of each sensor. These response values were acquired from four consecutive pulses upon exposure to each gas. To evaluate the influence of adding single sensors, data was gradually presented with the addition of a single sensor. The different gases cannot be discriminated by the pristine graphene sensor alone (Figure 4e-i). As the other data sets were obtained from the added Ag-, Au-, and Pt-decorated graphene sensors, each gas is well-separated in the principal component space (Figure 4e-ii,iii). This indicates that the sensor array possesses a high discrimination capability to the gases. In addition, the responses of the sensors exhibit different patterns in polar plots (Figure S15, Supporting Information). We compared our results with gas sensor arrays based on carbon materials in previous literatures (Table S4, Supporting Information). Our devices exhibit excellent gas discrimination capability with four sensors at room temperature using graphene microchannels with noble metal decoration. Relatively low gas concentrations were employed, which proves the superiority of this work. Furthermore, entirely flexible and transparent gas sensor arrays have not been achieved yet.[48,50–52]

For the Pt-decorated graphene sensor, the linear responses to hydrogen gas were detected for a wide range of gas concentrations, from 20 ppm to 1%, at 1 V without self-activation (**Figure 5**a). The responses of the sensor are 1.15%, 1.9%, 2.95%, 5%, 8.42%, 10.33%, 15.28%, 22.93%, 30.57%, and 39.66% to 20, 50, 100, 250, 500, 1000, 2500, 5000, 7500, 10 000 ppm of H_2.

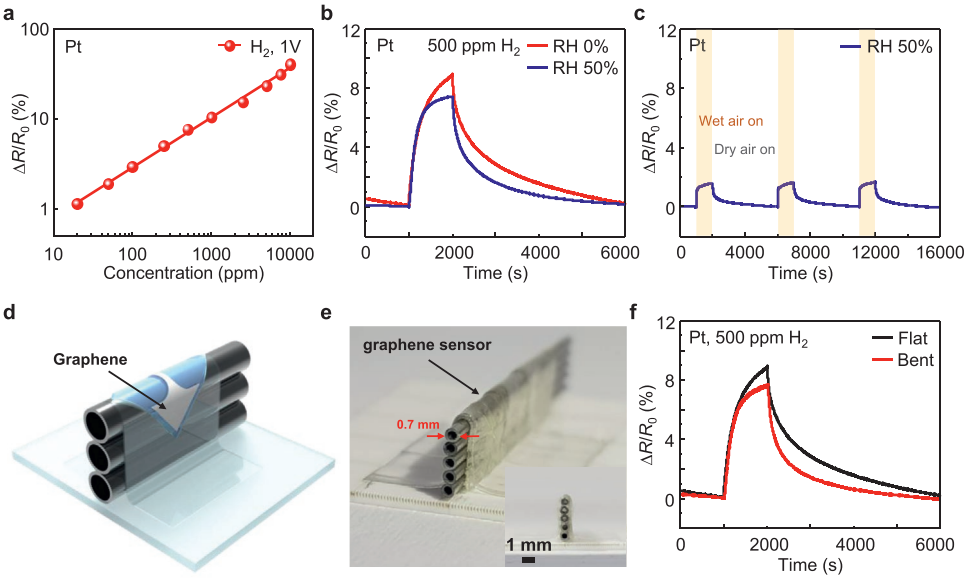

Figure 5. Hydrogen gas sensing properties of the Pt-decorated graphene sensor. a) Sensing responses of Pt-decorated graphene sensor upon exposure to hydrogen gas at 1 V. b) Response curves upon exposure to 500 ppm H_2 in 0% and 50% relative humidity atmosphere at 1 V. c) Response curves upon exposure to 50% relative humidity at 1 V. d) Schematic for the bent Pt-decorated graphene sensor. e) Optical image of the bent Pt-decorated graphene sensor. Inset shows a cross-sectional image of the device with bending radius of 0.5 mm. f) Sensing curves of Pt-decorated graphene sensor with and without mechanical bending.

The response as a function of the concentrations was plotted in a logarithmic scale and exhibited a linear relationship. To investigate the effect of humidity, the sensor was exposed to 500 ppm of H_2 in dry condition (0% relative humidity) and humidity condition (50% relative humidity) (Figure 5b). The responses in dry and wet condition are 8.42% and 7.45%, respectively. The degradation level, significantly lower than those of most semiconducting metal oxide-based gas sensors, is due to the low response of the graphene sensor to humidity by the hydrophobic nature of graphene, where the response to 50% relative humidity is as low as 1.58% (Figure 5c). Durability of the Pt-decorated sensors was examined under the mechanical bending strain. The bent sensor was attached to metal pipes and a polymer film with a bending radius of less than 0.5 mm (Figure 5d,e). The bent sensor showed a slightly deteriorated sensing curve with 500 ppm H_2 gas at 1 V compared with the curve of the flat sensor, but the sensing performance of the bent sensor was still reliable (Figure 5f). The high gas discrimination capability, endurance to humidity, and stability under high bending strain broadly expand the potential of the graphene sensor array for practical use.

We developed DPC transfer to stably define microscale patterns of graphene on large-scale flexible substrates. Graphene microchannels fabricated by DPC transfer on flexible substrates exhibited the self-heating effect up to ≈70 °C (apparently) under an applied bias voltage of 9 V. As graphene surfaces facing Cu foil are turned inside-out during DPC transfer, DPC transfer can provide a great opportunity to employ immaculate 2D material surfaces in flexible devices. To demonstrate the potential of DPC transfer in practical applications, an entirely flexible and transparent graphene gas sensor array was designed to discriminate gas species at room temperature. The DPC transfer demonstrated here is a facile and reliable approach to define micropatterns of 2D materials on large-scale transparent and flexible substrates. The results of this technique are required for next-generation electronic devices that are flexible, wearable, and foldable.

Experimental Section

Graphene Synthesis and Multiple Stacking Process: Graphene film was synthesized using a conventional chemical vapor deposition method using a high purity copper foil (99.99%) at 1000 °C with a hydrocarbon source (CH_4, 60 sccm) and hydrogen (H_2, 7 sccm) at 90 mTorr. The as-grown graphene/Cu film was coated with PMMA, and the graphene on the backside of the foil was removed by oxygen plasma using a reactive ion etcher. The Cu foil was etched by an APS solution. The PMMA/graphene layer was repeatedly transferred onto other graphene/Cu foils without additional PMMA coatings to obtain multiple-stacked graphene. Finally, the PMMA supporting polymer on the graphene was removed by acetone treatment.

Graphene Patterning and DPC Transfer: 3LG on the Cu foil was patterned by photolithography and O_2 plasma treatment (9 s) with 50 W plasma power. PI varnish was coated on top of the patterned graphene at 2000 rpm for 60 s. The spin-coated PI layer with the micropatterned graphene was thermally annealed to form a transparent PI film. For polymer curing, the temperature was slowly elevated from an initial temperature of 80 to 150 °C at a rate of 2 °C min^{-1} in a nitrogen atmosphere. The temperature was maintained for 30 min at 150 °C and elevated up to 300 °C at the same rate. After the polymer curing process, supporting films (TP3854, 3M) were thermally laminated on the cured polymer side at 90 °C. Finally, the Cu foil was etched by an APS solution to reveal graphene micropatterns.

Sensor Measurements: The gas sensing properties of the fabricated graphene sensors were measured without external heating. The temperature of the measurement system was not influenced by self-activation and maintained room temperature. As the flow gas was changed from dry air (21% oxygen and 79% nitrogen, without moisture) to a calibrated test gas (balanced with dry air), the variation in sensor resistance was monitored using a source measurement unit (Keithley 2365B). A constant flow rate of 1000 sccm was used for dry air and the test gas. The sensor resistance was measured under a DC bias voltage of 1–10 V. The response of the sensors ($\Delta R/R_0$) was accurately determined by measuring the baseline resistance of the sensors in dry air and the fully saturated resistance after exposure to the test gas. Gas flow was controlled using mass flow controllers, and all measurements were recorded to a computer over a general purpose interface bus interface. The current–voltage characteristics of the fabricated sensors were measured to check the ohmic behavior of the device.

Supporting Information

Supporting Information is available from the Wiley Online Library or from the author.

Acknowledgements

Y.K. and T.K. contributed equally to this work. This work was financially supported by the Ministry of Science and ICT (2020M2D8A206983011), the Basic Science Research Program (2017R1A2B3009135), and the Nano Material Technology Development Program (2016M3A7B4910) through the National Research Foundation of Korea (NRF). This work was also partly supported by the Technology development Program (S2939998) of the Ministry of SMEs and Startups (MSS, Korea) and performed, in part, at the Center for Integrated Nanotechnologies, an Office of Science User Facility operated for the U.S. Department of Energy (DOE) Office of Science. Los Alamos National Laboratory, an affirmative action equal opportunity employer, is managed by Triad National Security, LLC for the U.S. Department of Energy's NNSA, under contract 9233218CNA000001.

Conflict of Interest

The authors declare no conflict of interest.

Keywords

2D materials, chemical sensor arrays, finite element simulations, graphene, microscale patterning

Received: July 15, 2020
Revised: October 28, 2020
Published online: November 20, 2020

[1] K. S. Novoselov, V. I. Fal'ko, L. Colombo, P. R. Gellert, M. G. Schwab, K. Kim, *Nature* **2012**, *490*, 192.
[2] Y. H. Kim, J. S. Park, Y. Choi, S. Y. Park, S. Y. Lee, W. Sohn, Y. Shim, J. Lee, C. R. Park, Y. S. Choi, B. H. Hong, J. H. Lee, W. H. Lee, D. Lee, H. W. Jang, *J. Mater. Chem. A* **2017**, *5*, 19116.
[3] Y. Kim, Y. S. Choi, S. Y. Park, T. Kim, S. Hong, T. H. Lee, C. W. Moon, J. Lee, D. Lee, B. H. Hong, H. W. Jang, *Nanoscale* **2019**, *11*, 2966.
[4] K. S. Kim, Y. Zhao, H. Jang, S. Y. Lee, J. M. Kim, K. S. Kim, J. Ahn, P. Kim, J. Choi, B. H. Hong, *Nature* **2009**, *457*, 706.
[5] A. K. Geim, I. V. Grigorieva, *Nature* **2013**, *499*, 419.
[6] S. Bae, H. Kim, Y. Lee, X. Xu, J. Park, Y. Zheng, J. Balakrishnan, T. Lei, H. R. Kim, Y. I. Song, Y. Kim, K. S. Kim, B. Ozyilmaz, J. Ahn, B. H. Hong, S. Iijima, *Nat. Nanotechnol.* **2010**, *5*, 574.

[7] J. Ahn, B. H. Hong, *Nat. Nanotechnol.* **2014**, *9*, 737.
[8] Y. Dan, Y. Lu, N. J. Kybert, Z. Luo, A. T. C. Johnson, *Nano Lett.* **2009**, *9*, 1472.
[9] R. Stine, J. T. Robinson, P. E. Sheehan, C. R. Tamanaha, *Adv. Mater.* **2010**, *22*, 5297.
[10] M. M. Pour, A. Lashkov, A. Radocea, X. Liu, T. Sun, A. Lipatov, R. A. Korlacki, M. Shekhirev, N. R. Aluru, J. W. Lyding, V. Sysoev, A. Sinitskii, *Nat. Commun.* **2017**, *8*, 820.
[11] V. Strong, S. Dubin, M. F. El-Kady, A. Lech, Y. Wang, B. H. Weiller, R. B. Kaner, *ACS Nano* **2012**, *6*, 1395.
[12] D. Kong, L. T. Le, Y. Li, J. L. Zunino, W. Lee, *Langmuir* **2012**, *28*, 13467.
[13] T. Kim, H. Kim, S. W. Kwon, Y. Kim, W. K. Park, D. H. Yoon, A.-R. Jang, H. S. Shin, K. S. Suh, W. S. Yang, *Nano Lett.* **2012**, *12*, 743.
[14] Q. He, S. Wu, S. Gao, X. Cao, Z. Yin, H. Li, P. Chen, H. Zhang, *ACS Nano* **2011**, *5*, 5038.
[15] M. F. El-Kady, R. B. Kaner, *Nat. Commun.* **2013**, *4*, 1475.
[16] Q. He, H. G. Sudibya, Z. Yin, S. Wu, H. Li, F. Boey, W. Huang, P. Chen, H. Zhang, *ACS Nano* **2010**, *4*, 3201.
[17] F. Torrisi, T. Hasan, W. Wu, Z. Sun, A. Lombardo, T. S. Kulmala, G.-W. Hsieh, S. Jung, F. Bonaccorso, P. J. Paul, D. Chu, A. C. Ferrari, *ACS Nano* **2012**, *6*, 2992.
[18] K. Shin, J. Hong, J. Jang, *Adv. Mater.* **2011**, *23*, 2113.
[19] E. B. Secor, P. L. Prabhumirashi, K. Puntambekar, M. L. Geier, M. C. Hersam, *J. Phys. Chem. Lett.* **2013**, *4*, 1347.
[20] V. Dua, S. P. Surwade, S. Ammu, S. R. Agnihotra, S. Jain, K. E. Roberts, S. Park, R. S. Ruoff, S. K. Manohar, *Angew. Chem., Int. Ed.* **2010**, *49*, 2154.
[21] Y. H. Kim, S. J. Kim, Y. Kim, Y. Shim, S. Y. Kim, B. H. Hong, H. W. Jang, *ACS Nano* **2015**, *9*, 10453.
[22] Y. Yang, D. Yin, C. Zhong, R. Xiong, J. Shi, Z. Liu, X. Wang, Q. Lei, *Polym. Eng. Sci.* **2013**, *53*, 1536.
[23] A. C. Ferrari, D. M. Basko, *Nat. Nanotechnol.* **2013**, *8*, 235.
[24] Z. Zhang, J. Du, D. Zhang, H. Sun, L. Yin, L. Ma, J. Chen, D. Ma, H.-M. Cheng, W. Ren, *Nat. Commun.* **2017**, *8*, 14560.
[25] W. S. Leong, H. Wang, J. Yeo, F. J. Martin-Martinez, A. Zuhair, P.-C. Shen, Y. Mao, T. Palacios, M. J. Buehler, J.-Y. Hong, J. Kong, *Nat. Commun.* **2019**, *10*, 867.
[26] A. Pirkle, J. Chan, A. Venugopal, D. Hinojos, C. W. Magnuson, S. McDonnell, L. Colombo, E. M. Vogel, R. S. Ruoff, R. M. Wallace, *Appl. Phys. Lett.* **2011**, *99*, 122108.
[27] Y. Lin, C. Lu, C. Yeh, C. Jin, K. Suenaga, P. Chiu, *Nano Lett.* **2011**, *12*, 414.
[28] J. Kang, D. Shin, S. Bae, B. H. Hong, *Nanoscale* **2012**, *4*, 5527.
[29] M. Her, R. Beams, L. Novotny, *Phys. Lett. A* **2013**, *377*, 1455.
[30] C. Gong, H. C. Floresca, D. Hinojos, S. McDonnell, X. Qin, Y. Hao, S. Jandhyala, G. Mordi, J. Kim, L. Colombo, R. S. Ruoff, M. J. Kim, K. Cho, R. M. Wallace, Y. J. Chabal, *J. Phys. Chem. C* **2013**, *117*, 23000.
[31] D. Sui, Y. Huang, L. Huang, J. Liang, Y. Ma, Y. Chen, *Small* **2011**, *7*, 3186.
[32] N. Karim, M. Zhang, S. Afroj, V. Koncherry, P. Potluri, K. S. Novoselov, *RSC Adv.* **2018**, *8*, 16815.
[33] H. Sun, D. Chen, C. Ye, X. Li, D. Dai, Q. Yuan, K. W. A. Chee, P. Zhao, N. Jiang, C. Lin, *Appl. Surf. Sci.* **2018**, *435*, 809.
[34] M. W. Jung, S. Myung, W. Song, M. Kang, S. H. Kim, C. Yang, S. S. Lee, J. Lim, C. Park, J. Lee, K. An, *Appl. Mater. Interfaces* **2014**, *6*, 13319.
[35] C. Li, Y. Xu, B. Zhao, L. Jiang, S. Chen, J. Xu, X. Fu, R. Sun, C. Wong, *J. Mater. Sci.* **2016**, *51*, 1043.
[36] D. Kim, L. Zhu, D. Jeong, K. Chun, Y. Bang, S. Kim, J. Kim, S. Oh, *Carbon* **2013**, *63*, 530.
[37] Y.-H. Yoon, J.-W. Song, D. Kim, J. Kim, J.-K. Park, S.-K. Oh, C.-S. Han, *Adv. Mater.* **2007**, *19*, 4284.
[38] H. Jang, S. K. Jeon, S. H. Nahm, *Carbon* **2011**, *49*, 111.
[39] J. Kang, H. Kim, K. S. Kim, S. Lee, S. Bae, J. Ahn, Y. Kim, J. Choi, B. H. Hong, *Nano Lett.* **2011**, *11*, 5154.
[40] J. Lee, H. J. Bong, Y. Lee, D. Kim, M.-G. Lee, *Metall. Mater. Trans. A* **2019**, *50*, 2720.
[41] W. Lee, K. D. Kihm, H. G. Kim, S. Shin, C. Lee, J. S. Park, S. Cheon, O. M. Kwon, G. Lim, W. Lee, *Nano Lett.* **2017**, *17*, 2361.
[42] A. Y. Serov, Z. Ong, E. Pop, *Appl. Phys. Lett.* **2013**, *102*, 033104.
[43] S. Y. Park, Y. Kim, T. Kim, T. H. Eom, S. Y. Kim, H. W. Jang, *InfoMat* **2019**, *1*, 289.
[44] D. H. Wang, Y. Hu, J. J. Zhao, L. L. Zeng, X. M. Tao, W. Chen, *J. Mater. Chem. A* **2014**, *2*, 17415.
[45] F. Schedin, A. K. Geim, S. V. Morozov, E. W. Hill, P. Blake, M. I. Katsnelson, K. S. Novoselov, *Nat. Mater.* **2007**, *6*, 652.
[46] J.-W. Yoon, J.-H. Lee, *Lab Chip* **2017**, *17*, 3537.
[47] G. Zheng, F. Patolsky, Y. Cui, W. U. Wang, C. M. Lieber, *Nat. Biotechnol.* **2005**, *23*, 1294.
[48] A. Star, V. Joshi, S. Skarupo, D. Thomas, J.-C. P. Gabriel, *J. Phys. Chem. B* **2006**, *110*, 21014.
[49] N. A. Rakow, K. S. Suslick, *Nature* **2000**, *406*, 710.
[50] C. Shi, H. Ye, H. Wang, D. E. Ioannou, Q. Li, *Appl. Phys. Lett.* **2018**, *113*, 222102.
[51] S. F. Liu, L. C. H. Moh, T. M. Swager, *Chem. Mater.* **2015**, *27*, 3560.
[52] M. S. Wiederoder, E. C. Nallon, M. Weiss, S. K. McGraw, V. P. Schnee, C. J. Bright, M. P. Polcha, R. Pafferroth, J. R. Uzarski, *ACS Sens.* **2017**, *2*, 1669.